European Journal of Medicinal Chemistry 156 (2018) 747–759

Contents lists available at ScienceDirect

European Journal of Medicinal Chemistry

journal homepage: http://www.elsevier.com/locate/ejmech

Research paper

Novel ruthenium(II) triazine complex $[Ru(bdpta)(tpy)]^{2+}$ co-targeting drug resistant GRP78 and subcellular organelles in cancer stem cells

Baskaran Purushothaman [1], Parthasarathy Arumugam [1], Hee Ju, Goutam Kulsi, Annie Agnes Suganya Samson, Joon Myong Song*

College of Pharmacy, Seoul National University, Seoul 151-742, South Korea

ARTICLE INFO

Article history:
Received 9 April 2018
Received in revised form
14 July 2018
Accepted 17 July 2018
Available online 20 July 2018

Keywords:
Ruthenium(II) complex
Cancer stem cells
Glucose regulated protein 78
Mitochondria
Apoptosis

ABSTRACT

Ruthenium(II/III) metal complexes have been widely recognized as the alternative chemotherapeutic agents to overcome the drug resistance and tumor recurrence associated with platinum derivatives. In this work, a novel ruthenium(II) triazine complex namely, **1** ($[Ru(bdpta)(tpy)]^{2+}$) was synthesized and spectroscopically characterized. Drug resistant cancer stem cells (CSCs) were used to evaluate the cytotoxicity of Ru(II) complex **1**. The complex **1** showed a greater cytotoxic potential with IC_{50} values lower than that of cisplatin. The intracellular localization assay confirmed that the complex **1** was effectively distributed into mitochondria as well as endoplasmic reticulum (ER), and executed a ROS-mediated calcium and Bax/Bak dependent intrinsic apoptosis. Interestingly, direct interaction between complex **1** and glucose regulated protein 78 (GRP78), a protein associated with drug resistance caused the ROS-mediated ubiquitination of GRP78. Notably, western blot and confocal microscopy analysis confirmed that complex **1** significantly reduced the protein levels of GRP78. Dose-dependent *in vivo* antitumor efficacy against CD133+HCT-116 CSCs derived tumor xenograft further validated that complex **1** could be an effective chemotherapeutic agent.

1. Introduction

Platinum based cisplatin derivatives such as cisplatin, carboplatin and oxaliplatin are the commonly employed chemotherapeutic drugs against solid tumours such as testicular, head and neck, bladder, ovarian, and lung cancers [1,2]. However, long-term administration of platinum derivatives results in side effects, as well as drug resistance and subsequently relapse of cancer [3–5]. In search of potential alternatives to the platinum derivatives, ruthenium based metal complexes have emerged as a potential contender to platinum derivatives [6,7]. Recent *in-vitro* and *in-vivo* studies on ruthenium(II, III) metal complexes indicated that derivatives of ruthenium metal complexes could resolve the issues such as side effects and drug resistance in cancer [8–14]. Ruthenium(III) complex exhibits a strong affinity towards serum albumin and transferrin, this property ensures the smooth transportation of ruthenium complex across the vascular system [15–17]. Rapidly dividing cells express the elevated levels of transferrin due to the higher requirement of iron. It has previously been reported that the expression of iron transport proteins such as transferrin and ferritin were increased in metastasis cancer [18,19]. Hence, ruthenium(II, III) complexes are more likely to accumulate in cancer tissue. After a successful preclinical studies, NAMI-A, the first ruthenium(III) complex has completed the phase-I/II clinical trials in combination with gemcitabine in non-small cell lung cancer (NSCLC) patients. However, the trial was unsuccessful due to the side effects and less activity of NAMI-A in NSCLC [20,21]. The disappointing results of NAMI-A necessitate the design of new ruthenium complexes in the field of anti-cancer drug discovery. In the present work, we have synthesized a novel ruthenium(II) complex with specific ligand to overcome multidrug resistance in cancer stem cells (CSCs), namely ruthenium(II) triazine complex **1** ($[Ru(bdpta)(tpy)]^{2+}$). The tridentate ligand 4-(4,6-bis(3,5-dimethyl-1H-pyrazole-1-yl)-1,3,5,-triazine-2-yl)-N,N-diethylaniline (**bdpta**) was used in the synthesis of ruthenium(II) complex **1**. In our design, the pyrazolyl-1,3,5-triazine (**bdpta**) was taken as a core component and it acts as chelating ligand to synthesize complex **1**. The 1,3,5-triazine chemical core based compounds have been used as anticancer agents for many groups [22–24]. Few

* Corresponding author.
E-mail address: jmsong@snu.ac.kr (J.M. Song).
[1] These authors contributed equally to this work.

https://doi.org/10.1016/j.ejmech.2018.07.048
0223-5234/

ruthenium complexes containing 1,3,5-triazine ligand were reported and their redox behaviour and luminescence properties were studied [25,26]. However, no attention has been focused on the ruthenium(II) complexes containing a pyrazolyl-1,3,5-triazine core as an anticancer agent, targeting subcellular organelles as well as drug resistant proteins. Inspired by these findings our attention was focused on the synthesis of novel Ru(II) complexes with ligands targeting subcellular organelles. The complex **1** containing *N,N*-diethylaniline moiety in 1,3,5-triazine core targets mitochondria in cancer stem cells. Similarly, a polypyridyl group of the complex **1** helps to accumulate in endoplasmic reticulum (ER) due to its lipophilic nature [27].

The newly synthesized Ru(II) complex **1** was characterized by spectroscopic methods and their cytotoxicity was evaluated using a cancer cell lines as well as CSCs. The CSCs was chosen as an *in vitro* model to study the cytotoxicity, sub-cellular localization, drug resistance and other molecular mechanisms pertaining to the ruthenium(II) complex. For this purpose, CD133+ MCF-7 cells and CD133+ HCT-116 cells were used. Cancer cells which expressing CD44 and CD133 markers are widely recognized as CSCs. A number of reports indicated that cisplatin resistance cancer cell lines expressed significant levels of stem cell markers such as CD133 and CD44 [28]. In addition, CSCs are widely considered for the recurrence of cancer since they express high levels of proteins associated with drug resistance and cell survival mechanism [29]. Hence, the CSCs model is an ideal model to evaluate the efficacy of drug pertaining to drug resistance. It has been reported that the ROS induced oxidation process can bring conformational changes to protein and its side chain amino acids, which leads to the ubiquitination of modified protein [30,31]. Due to the ROS generating ability of the complex **1**, its ROS mediated direct effect on the proteins associated with drug resistance mechanism such as GRP-78, clusterin (CLU), and ataxia telangiectasia and Rad3-related protein (ATR) were analysed. GRP78, a major molecular chaperon in the ER, was demonstrated in the drug resistance, stemness characteristics of cancer cells and the recurrence of cancer [32,33]. Clusterin is an anti-apoptotic protein, elevated expression of clusterin has been reported in the paclitaxel/docetaxel resistance in prostate, breast and lung cancer [34,35]. ATR is a cell cycle regulating protein, it has been demonstrated that suppression of ATR stimulates the malignant cells to apoptosis [36]. In addition, the *in vivo* efficacy of complex **1** was evaluated using CD133+HCT-116 CSCs induced tumor xenograft mice model. This work, to the best of our knowledge, presents a detailed biological evaluation of a multi-targeting ruthenium(II) triazine complex **1** on CSCs by *in vitro*, as well as *in vivo* model.

2. Results and discussion

2.1. Synthesis and characterization of Ru(II) complex 1

The ligand 4-(4,6-bis(3,5-dimethyl-1H-pyrazole-1-yl)-1,3,5,-triazine-2-yl)-N,N-diethylaniline (**bdpta**) was prepared using a previously described method and it is explained in detail in the supporting information [37,38]. The ruthenium(II) complex **1** was synthesized with their corresponding ligand (bdpta). The synthetic protocol for Ru(II) complex **1** is represented in Scheme 1. The $[Ru(tpy)Cl_3]$ (**iv**) was prepared by refluxing the equivalent molar ratio of 2,2′:6′,2″-terpyridine (**iii**) and $RuCl_3 \cdot 3H_2O$ in ethanol at 80 °C for 3 h. The complex **1** was synthesized from an equal molar ratio of $[Ru(tpy)Cl_3]$ and **bdpta** in ethylene glycol at 170 °C overnight under nitrogen protection. This was followed by anion exchange with $NaClO_4$ and purification by column chromatography with CH_3CN and 10% KNO_3 as an eluent. The complex **1** was isolated as brown solid. The stability of the synthesized Ru(II) complex **1** was checked by dissolving the compound in PBS buffer and kept at room temperature for 24 h. No obvious change was observed, and this was further confirmed by using UV-Vis absorption spectroscopy. The UV-Vis absorption and emission spectrum of ruthenium(II) complex **1** were measured in acetonitrile (See Fig. S1). The electronic absorption spectrum for the Ru(II) complex **1** display high energy bands at 396 nm, due to ligand-centered π-π*

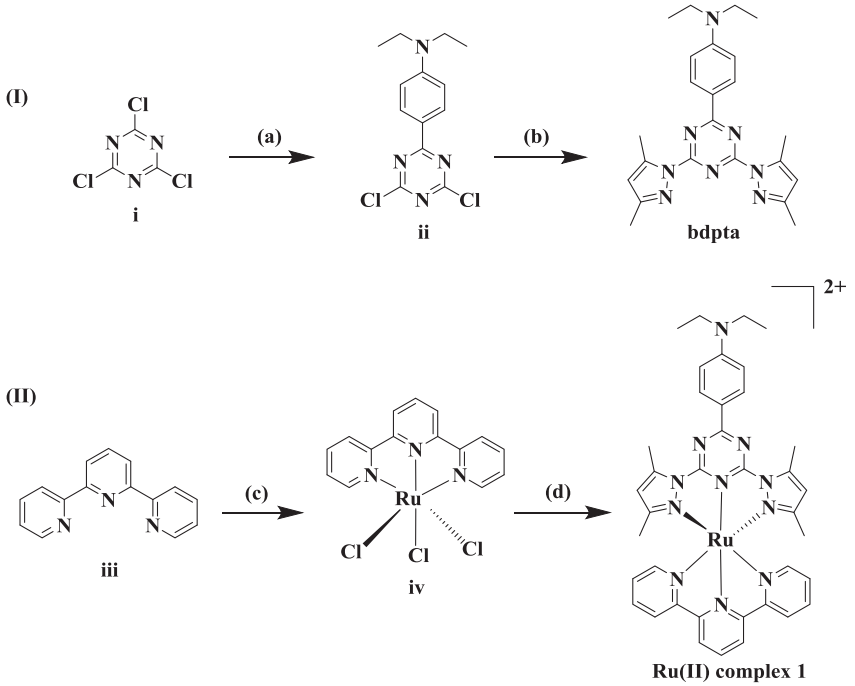

Scheme 1. Synthesis of Ru(II) complex **1**; Reagents and conditions: (a) *N,N*-diethylaniline, 75 °C, 8 h; (b) 3,5-dimethylpyrazole, K metal, THF, reflux, 8 h; (c) $RuCl_3 \cdot 3H_2O$, ethanol, reflux, 3 h; (d) bdpta, ethylene glycol, N_2, reflux, 16 h.

Table 1
IC_{50} value for complex **1** and *cisplatin* against MCF-7 and HCT-116 cancer cells, CD44+MCF-7 and CD133+HCT-116 CSCs.[a]

Complex Name	IC_{50} Values (μM)			
	MCF-7	CD44+MCF-7	HCT-116	CD44+HCT-116
Ru(II) complex **1**	2.1 ± 0.06	3.48 ± 0.07	2.62 ± 0.05	3.89 ± 0.09
Cisplatin	5.1 ± 0.23	8.63 ± 0.42	6.01 ± 0.49	11.14 ± 0.7

[a] Cell viability was determined by SRB assay after 48 h incubation (mean of three independent experiments ± SD).

transitions. The broad and low energy absorbance between 515 nm are characteristic of metal-to-ligand charge-transfer (MLCT) transitions from the Ru(II) metal centre to the polypyridyl ligand.

The ^{1}H NMR spectra of complex **1** in CD_3OD show downfield shifts in the positions of aromatic protons due to the incorporation of terpyridine and bdpta ligands that were observed between δ = 10.38 ppm and δ = 6.52 ppm. The aliphatic protons of N,N-diethylaniline and pyrazole group in the complex **1** show upfield shifts in the spectrum, which were observed between δ = 6.52 ppm and δ = 1.32 ppm. The characteristic peaks of pyrazole C-H in complex **1** show at 6.31 ppm and aromatic protons of N,N-diethylaniline show at 8.43–8.36 and 6.97–6.89 ppm. The ligand and Ru(II) complex **1** was characterized by ^{1}H, ^{13}C NMR, MALDI-TOF MS, UV-Vis spectroscopy and reported in Supplementary Figs. S8–S12.

2.2. Cytotoxicity activity studies of Ru(II) complex 1

The cytotoxicity of Ru(II) complex **1** was evaluated by sulforhodamine B (SRB) assay using a set of cancer cell lines (MCF-7 and HCT-116 cell line) and CSCs (CD44 + MCF7 and CD133 + HCT116 cells). Cisplatin was used as a positive control. Table 1 depicts the IC_{50} values of complex **1,** and *cisplatin* against the above-mentioned cancer cell lines. In our present work, the cytotoxicity study shows that the complex **1** was more potent than the cisplatin under condition at 48 h treatment. Notably, the IC_{50} value of complex **1** for all the cell lines and CSCs used in the study was much lower than cisplatin. Efficacy of the cytotoxic activities observed in the following order: **1** > *cisplatin*. The IC_{50} values of complex **1** against MCF-7, CD44+MCF-7, HCT-116, and CD133+HCT-116 cell lines are 2.1 ± 0.06 μM, 3.48 ± 0.07 μM, 2.62 ± 0.05 μM, and 3.89 ± 0.09 μM respectively (Table 1). Significantly higher IC_{50} values against CSCs were observed as compared to the cancer cells. It should be considered that CSCs generates relatively low levels of ROS as compared to the cancer cells [39]. In addition, CSCs expresses elevated levels of antioxidant enzymes [40]. In the present study, as compared to the *cisplatin*, complex **1** showed two to threefold efficacy against cancer cell lines and cancer stem cells.

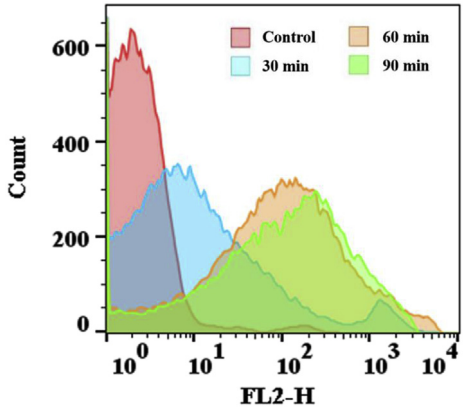

Fig. 1. FACS analysis shows the uptake of the Ru(II) complex **1** by CD44+MCF-7 cells at different time points (30, 60 and 90 min). Cells were treated with 10 μM of complex **1**.

2.3. The cellular uptake and subcellular localization of Ru(II) complex 1

Successful chemotherapeutic efficacy of anticancer drug is mostly dependent on the cellular uptake and accumulation in intracellular organelles. To assess the levels of cellular uptake of the Ru(II) complex **1**, CD44+MCF-7 cells were treated with 10 μM of complex **1**, and their intracellular fluorescence intensity was investigated at 620 nm by FACS at different time intervals (30, 60, and 90 min) (Fig. 1). The results herein show that the fluorescence intensity of complex **1** was gradually increased from 30 min onwards and attained saturation at 60 min. The observed fluorescence intensity of complex **1** within 30 min suggests a rapid cellular uptake by MCF-7 CSCs. In order to analyse the mechanism of action of the complex **1**, subcellular localization assays were performed in CD133+HCT-116 C SCs using organelle-specific dyes. Mito-tracker red and ER tracker red dyes were used to assess the accumulation of complex **1** in mitochondria (Fig. 2A) and ER (See Fig. 2B) respectively. In addition, Hoechst dye was used for nuclear entry. The overlapping confocal fluorescence microscopy images clearly indicated that the complex **1** mostly distributed in mitochondria as well as ER in the cytoplasm of CD133+HCT-116 cells. Subcellular localization assay of complex **1** was also performed in CD44+MCF-7 cells and confirmed that complex **1** effectively distributed in mitochondria and ER (See Supplementary Fig. S2). These results further showed that the complex **1** was poorly distributed in the nucleus. The observed results indicated that the ER dependent mitochondria mediated apoptotic pathway could be the mode of action of the complex **1**.

2.4. Ruthenium(II) complex 1 induces ROS in cancer stem cells

Accumulation of transition metal complexes like ruthenium(II) complex **1** in mitochondria or ER can effectively generate reactive oxygen species (ROS) through Fenton type redox reactions [41]. Redox cycling is an important characteristic of transition metals, this property enables the transition metals to simultaneously inactivate the antioxidant proteins and also generate the free radicals in the cancer cells under an acidic microenvironment [42]. Excessive ROS generation is one of the characteristic features of cancer cells. Increased metabolic activity of peroxisomes and mitochondria are the major contributors of ROS in tumor. Cancer cells effectively utilize the ROS for their cell proliferation, angiogenesis, and metastasis progression [43]. Cancer cells can delicately balance the excessive ROS by increasing the expression of antioxidant proteins such as glutathione and thioredoxin [44,45]. Hence, cancer cells can withstand metabolic and pharmacological insults up to their threshold limit of ROS toxicity. In addition, it is well proven that CSCs synthesize high levels of antioxidant enzyme as well as non-enzyme anti-oxidant proteins, compared to the proliferative cancer cells [46,47]. This survival mechanism enables the CSCs to develop drug resistance against chemotherapeutic drugs. Treatment strategies such as simultaneously increasing the ROS generation as well as suppressing the anti-oxidant potential of the cancer cell, can lead to irreversible oxidative stress and subsequent apoptosis. Earlier studies indicated that the inhibition of certain antioxidant systems can effectively kill cancer cells through an apoptotic cell death mechanism by elevating the ROS levels behind the threshold limit of cancer cells [48,49]. It has been reported that ruthenium(II) polypyridyl complexes can markedly increase the

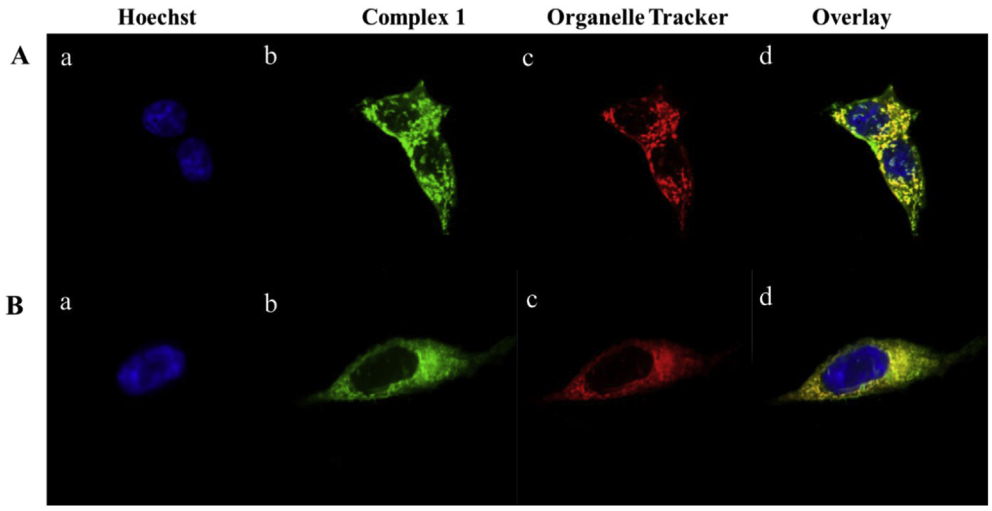

Fig. 2. Subcellular localization of complex **1** in CD133+HCT-116 cells. Cells were treated with 10 μM of complex **1** for 1 h at 37 °C in a humidified atmosphere of 5% CO_2. (A) Mitochondrial localization: a) Nuclear staining, b) Emission of complex **1**, c) Emission of Mito-tracker red, d) The merged images. (B) Localization of endoplasmic reticulum: a) Nuclear staining, b) Emission of complex **1** (green), c) Emission of ER-tracker red, d) the merged images. (For interpretation of the references to colour in this figure legend, the reader is referred to the Web version of this article.)

intracellular ROS level [14,50]. In the present study, we observed an elevated ROS generation in CSCs of HCT-116 and MCF-7 in a concentration dependent manner (0, 1, 2, and 3 μM) within 6 h of complex **1** treatment (Fig. 3). Fig. 3A shows the 2′,7′-dichlorofluorescein diacetate (DCFH-DA) staining of complex **1** treated CSCs of HCT-116 and MCF-7 cell lines. Oxidation-sensitive DCFH-DA generates green fluorescence in the presence of ROS. Fig. 3B depicts the average fluorescence intensity of DCFH-DA staining at different concentrations of complex **1** treated cells. Due to the efficiency in ROS generation, the complex **1** exhibited good cytotoxic potential, irrespective of cell types, including CSCs of HCT-116 and MCF-7.

2.5. High-content cell death dynamics and evaluation of the MPT, cytosolic calcium, caspase3/7

The interplay between ROS and calcium homeostasis and their combined role in cell death pathways have been well established in cancer cells. The ER lumen is a major storage of intracellular Ca^{2+}. Moreover, Ca^{2+} is necessary for the proper activation of a number of molecular chaperones such as GRP-78 [51,52]. Therefore, fluctuations of Ca^{2+} levels in the ER can severely impact protein folding capacities. Oxidative stress due to enhanced ROS levels causes a Ca^{2+} influx into the cytoplasm from ER, or sarcoplasmic reticulum (SR) through the ER/SR-localized channels [53]. The acute release of Ca^{2+} from the ER can trigger a variety of signaling mechanisms that promote cell death, mainly via mitochondrial modulation [54,55]. The cellular localization study clearly indicated that the ruthenium(II) complex **1** is mostly distributed in mitochondria and ER. Hence, complex **1** induced ROS could mediate calcium release from ER, which could play a role in the activation of caspase mediated apoptosis. To find the mechanism of complex **1** mediated cell cytotoxicity high content assay was employed as previously demonstrated in our lab to assess the induction of mitochondrial permeability transition pore (MPTP) to the inner mitochondrial membrane, cytosolic calcium level and the activation of caspase-3 [56]. Fig. 4 represents the cell death mechanism of complex **1** in

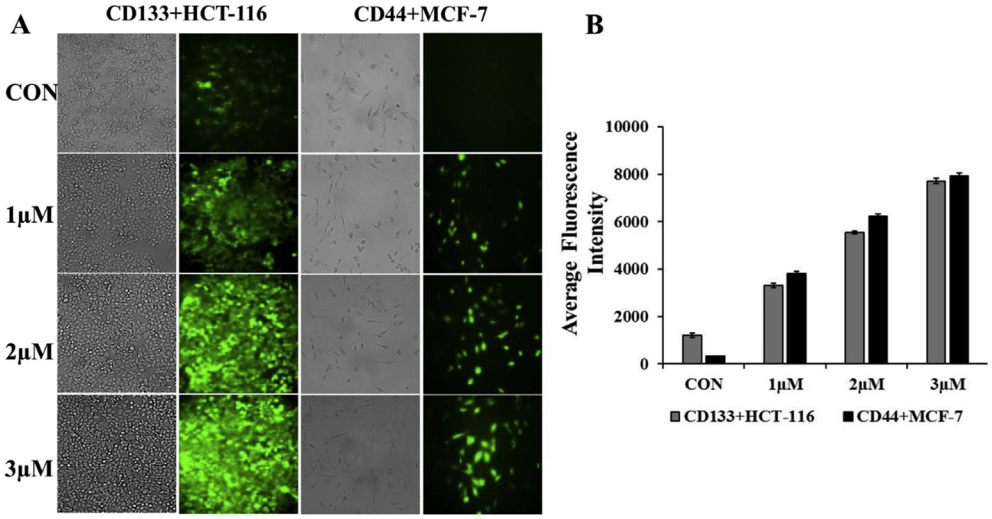

Fig. 3. (A) Intracellular ROS generation in complex **1** treated CD44+MCF-7 and CD133+HCT-116 cells. Cells were treated with different concentrations of complex **1** (1, 2 and 3 μM) for 6 h, at 37 °C in a humidified atmosphere of 5% CO_2. (B) Bar graph represents the average fluorescence intensity of 2′,7′-dichlorofluorescin diacetate. Error bars represent the standard deviation of three independent measurements. (**P < 0.01, ***P < 0.001Vs Control).

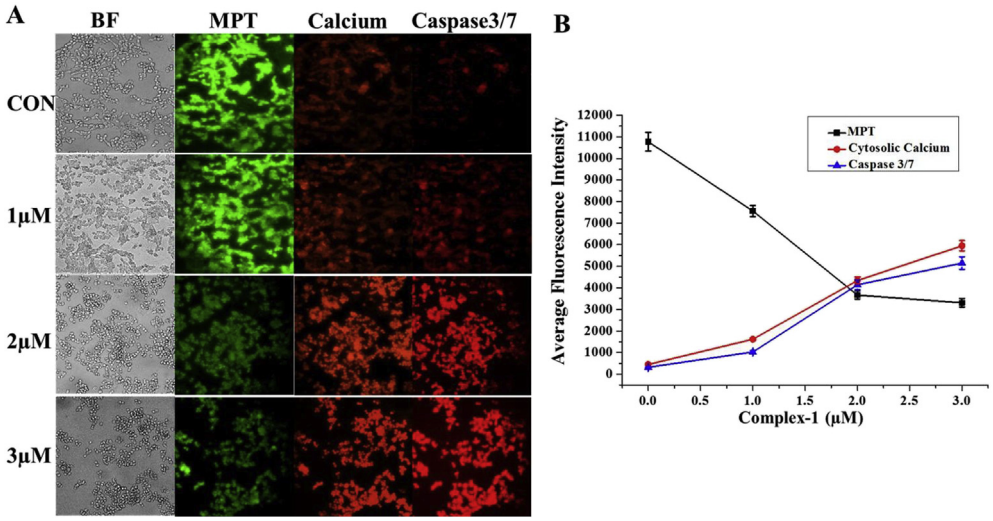

Fig. 4. High-content assay to find MPTP, Cytosolic calcium and caspase 3/7 in complex **1** treated CD133+HCT-116 cells, performed using AOTF. Cancer cells were treated with different concentration of complex **1** (0, 1, 2 and 3 μM) for 16 h at 37 °C in a humidified atmosphere of 5% CO_2. Fluorescent emission of Calcein AM, Calcium orange, and Magic red caspase 3/7 was monitored at 525 nm, 580 nm, and 630 nm respectively using AOTF. (A) The green fluorescent images correspond to cellular images of MPT, orange fluorescent images represent cytosolic calcium, and red fluorescent image represents caspase- 3/7. (B) Bar graph represents the average fluorescence intensity of Calcein AM, calcium indicator orange and caspase 3/7. (For interpretation of the references to colour in this figure legend, the reader is referred to the Web version of this article.)

CSCs of HCT-116. MPTP was assessed by measuring the fluorescence intensity of Calcein AM translocated into the mitochondria. However, $CoCl_2$ used in the study can enter and quench the Calcein AM only in the presence of MPTP. Hence, the fluorescence intensity of Calcein AM is indirectly proportional to the levels of MPTP. The observed results show that treatment of complex **1** drastically reduced the fluorescence intensity of the Calcein-AM accumulated in the mitochondria of CSCs in a concentration dependent manner compared to the control. A sharp reduction in the fluorescence intensity of the Calcein-AM accumulated in mitochondria was observed from 1 μM of complex **1** treatment and it was saturated at 2 μM of complex **1**. The MPTP formation on the inner mitochondrial membrane causes membrane depolarization, matrix swelling, and a rupture of outer membrane. It collectively causes the release of Cyt-c and the subsequent activation of caspase-3. The result observed herein shows an increased level of cytosolic calcium and caspase-3 activation in a concentration dependent manner in response to the complex **1** treatment.

2.6. Expression of pro-apoptotic Bax and Bak in complex 1 treated CD133+HCT-116 C SCs

ER stress response critically regulates the formation of MPTP. It has been generally speculated that calcium released from ER and subsequent increased cytosolic calcium generally stimulates the MPTP formation in mitochondria adjacent to the ER alone. However, activation and subsequent oligomerization of pro-apoptotic proteins such as Bak and Bax on the outer mitochondrial

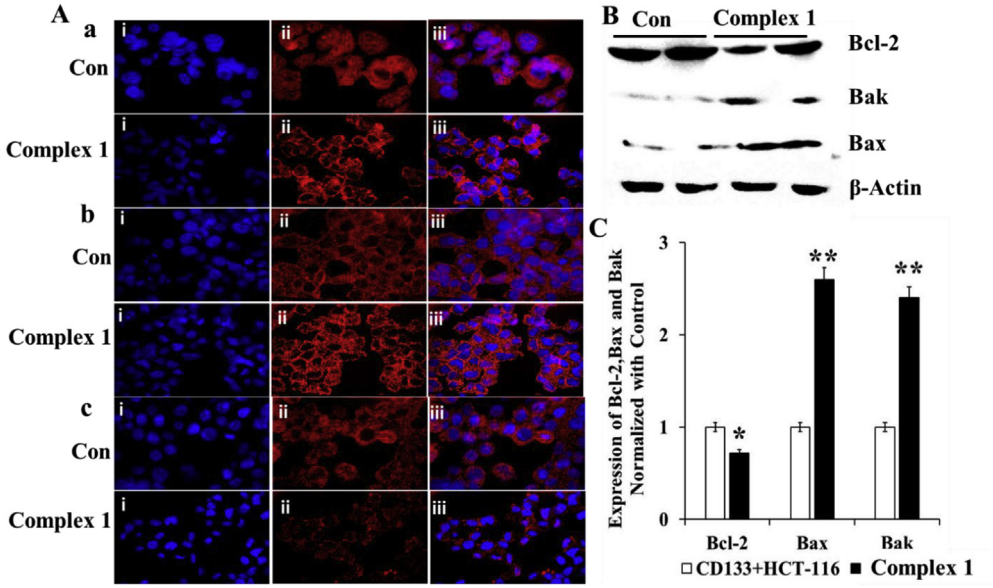

Fig. 5. (A) Expression of pro and anti-apoptotic proteins in complex **1** treated CD133+HCT-116 C SCs. a. Expression of Bax b. Expression of Bak c. Expression of Bcl-2 (i- DAPI, ii-Bax/Bak/Bcl-2, iii- Overlay). (B) Western blot analysis of Bcl-2, Bak, and Bax, respectively, in control and complex **1** treated cells. (C) Graph represents the relative expression of Bcl-2, Bax and Bak with control. Error bars represent the standard deviation of three independent measurements (*P < 0. **P < 0.01, Vs Control).

membrane stimulates the intrinsic apoptosis independent of calcium release [55]. Oligomerization of Bak/Bax leads to MOMP which causes the release of cytochrome c (Cyt c). In the cytosol, Cyt c activates the caspase-3 and caspase-7, the major effectors of apoptosis [54,57,58]. It has to be noted that MOMP is a point of no return for cell survival. In the present study, Fig. 5A–a and A-b represent the expression of Bax and Bak in control and complex **1** treated CSCs respectively. Oligomerized structures of Bax and Bak was observed in complex **1** treated cells. However, the oligomerization of Bax and Bak was poorly observed in control cells. Fig. 5B represents the western blot analysis of Bak and Bax. Significantly increased ($p < 0.01$) Bax and Bak levels were observed in complex **1** treated CSCs compared to the control. Moreover, Fig. 5 A-c represents the immunofluorescence analysis of anti-apoptotic protein Bcl-2 expression in control and complex **1** treated HCT-116 C SCs. The protein level of Bcl-2 was further assessed by western blot method and represented in Fig. 5B and C. The result shows that Bcl-2 expression was significantly suppressed in complex **1** treated CSCs ($p < 0.01$) as compared to the control. The observed reduced anti-apoptotic Bcl-2 expression in complex **1** treated cells can maintain the outflow of the Cyt-c release from the mitochondria. In addition, it has been reported that activated Bax positively regulates calcium release from the ER [59,60]. A transient overexpression of Bax results in the release of ER Ca^{2+} with a subsequent increase in mitochondrial Ca^{2+} and enhanced Cyt c release [61]. In contrast, cells with deficiency of both Bax and Bak have reduced Ca^{2+} release from ER [62–64]. Herein, observed results confirmed that complex **1** induced both MPTP and MOMP formation in mitochondria of cancer cells and ensures an effective intrinsic apoptosis mediated killing of cancer cells.

2.7. Ruthenium(II) complex 1 suppress GRP-78 levels in cancer stem cells

Considering the ROS generating ability of the complex **1**, it allows us to speculate that the complex **1** can influence the ROS dependent conformational changes on proteins closely associated with drug resistance. Initially, the effect of complex **1** on the proteins associated with drug resistance such as GRP-78, CLU, and ATR were analysed. The GRP-78, CLU, and ATR were cloned with YFP, RFP, and GFP bearing plasmids, respectively and were separately transfected into HEK-293 cells. The GRP-78, CLU, and ATR overexpressed HEK-293 cells were treated with complex **1** at concentrations of 1, 2, 3, 4, and 5 μM for 16 h and then fluorescence intensity of fluoroproteins were observed. Interestingly, in response to the complex **1** treatment, a dose dependent reduced expression of GRP-78 was observed, while the remaining two proteins were not decreased compared to the control (Fig. 6). However, significance differences in m-RNA levels of GRP78 were not observed between control and complex **1** treated CSCs (Fig. 6D). This leads to the conclusion that a direct interaction between GRP78 and ruthenium complex **1** could degrade the GRP-78 protein via ROS induced

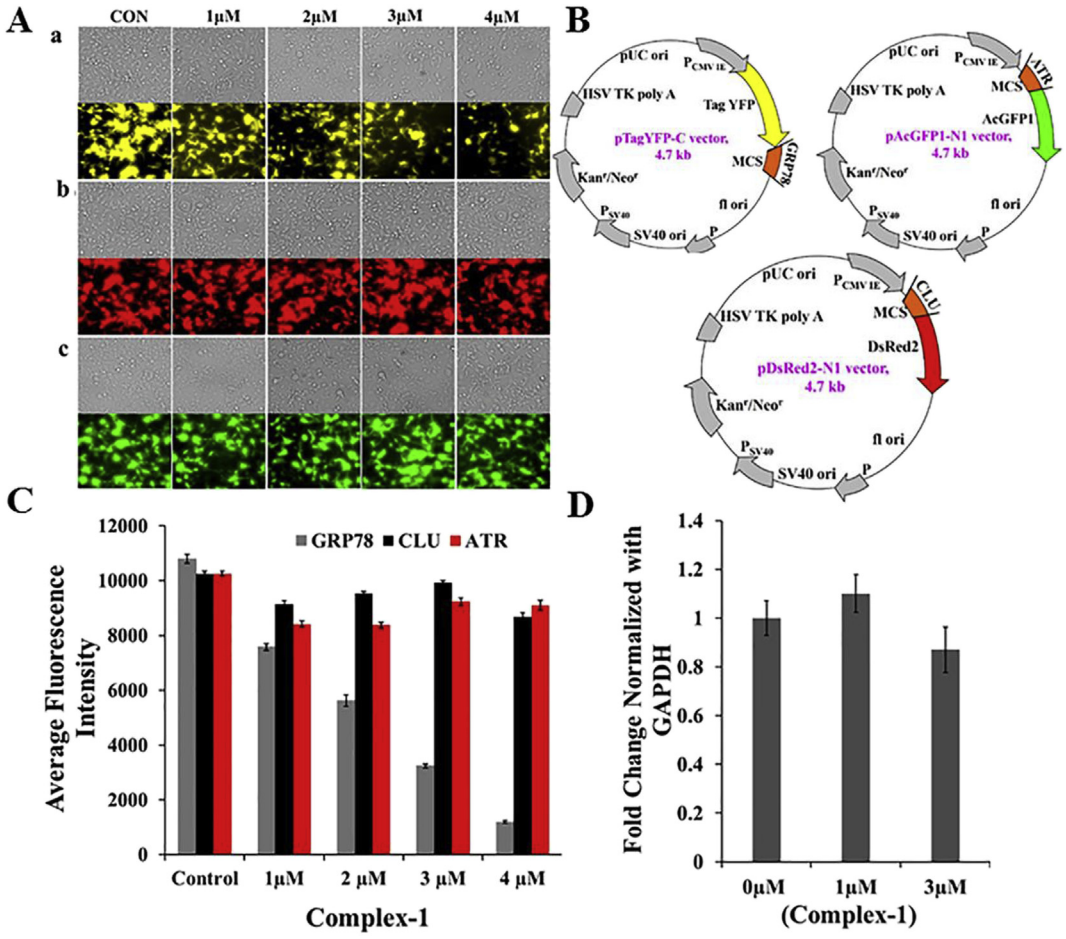

Fig. 6. (A) Expression of (a) GRP78 (b) Clusterin (c) ATR in response to the different concentration of complex **1** in pTag-YFP-GRP78-C, pDs-CLU-Red2-N1 and pAC-ATR-GFP1-N1 transfected HEK293 cells. (B) Vector design of pTag-YFP-GRP78-C, pDs-CLU-Red2-N1 and pAC-ATR-GFP1-N1. (C) Bar graph represents the average fluorescence intensity of GFP, RFP and GFP in plasmid transfected HEK293 cells at different concentration of complex **1**. (D) mRNA expression of GRP78 in complex **1** treated CD133+HCT-116 cells. The mRNA expression was analysed by RT-PCR. (For interpretation of the references to colour in this figure legend, the reader is referred to the Web version of this article.)

modifications. It has previously been reported that an ROS induced oxidation process can induce conformational changes in protein and make them prone to ubiquitination [30,31]. To confirm this, molecular docking was performed with an X-ray crystal structure of GRP 78 (PDB: 3ldl) using Accelrys Discovery Studio (v 4.0). The docking results revealed that complex **1** did not interfere with the function of the ATP domain of GRP78. However, the ruthenium complex **1** formed a strong non-covalent interaction with specific amino acid residues of GRP-78 at the interface of the dimeric structure of the protein, thereby intercalating between the dimeric structures of GRP-78 (Fig. 8). The observed docking results implied that the ROS generated in the vicinity of the complex **1** and GRP-78 interface could modify the conformation of GRP78 and subsequently its ubiquitin mediated lysis. Confocal analysis of the present study confirmed that the maximum of GRP-78 expression overlapped within the ER region. In addition, it showed that GRP78 expression was reduced in accordance with the concentration of complex **1** (Fig. 7 and Supplementary Fig. S4). It has to be noted that the lifetime of ROS is in the microseconds, hence its effect will be more in the vicinity where it has existed. This allowed us to conclude that the binding of complex **1** with GRP-78 could inflict conformational changes to the GRP-78 which leads to its ubiquitin mediated degradation. Western blot analysis also confirmed that complex **1** dose dependently reduced the protein levels of GRP-78 (Fig. 7C and D). Earlier, elevated levels of GRP-78 expression were evidenced in CD44+MCF-7 cells, compared to their normal counterpart. Chiu et al. reported that CD24−CD44 + Grp78 + cells exhibited superior chemo and radio resistance compared with CD24−CD44 $^{+}$ cells in head and neck cancer cell lines [65]. Similarly, the knock down of GRP78 has been implicated in the improved sensitivity to chemo and radio therapy [66]. This clearly suggests that the suppressive effect of complex **1** against GRP-78 is a highly advantageous property that can reduce the chances of tumor recurrence in cancer treatment.

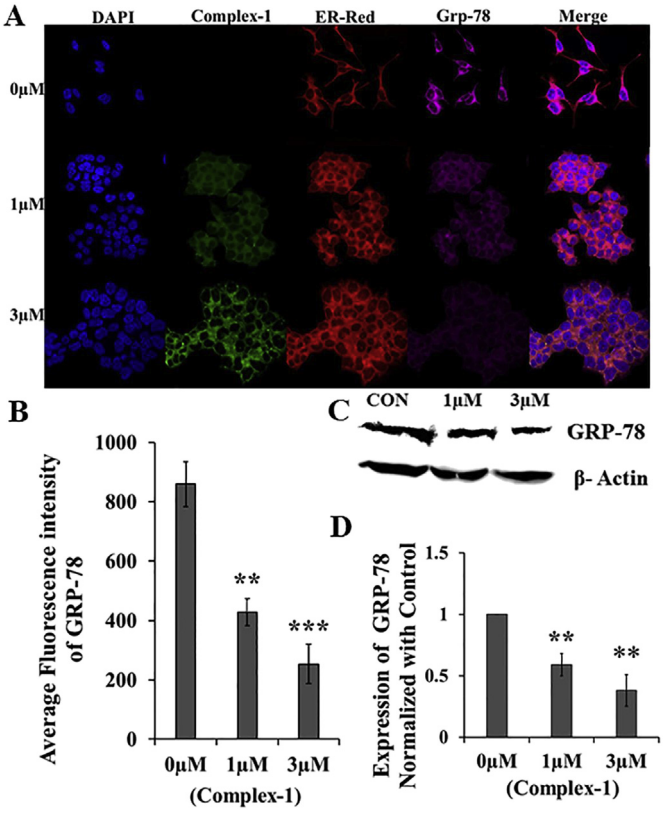

Fig. 7. (A) Expression of GRP78 in control and complex **1** (0, 1 and 3 μM) treated CD133+HCT-116 cells. Fluorescence expression of GRP-78 was merged with the fluorescence expression of ER tracker red. (B) Bar graph represents the average fluorescence intensity of GRP-78 in CD133 + HCT cancer cells treated with different concentrations of complex **1**. (C) Western blot represents the expression of GRP78 in control and complex **1** treated CD133+HCT-116 cells. (D) Bar graph represents the relative expression of GRP-78 with control. Error bars represent the standard deviation of three independent measurements (**P < 0.01, Vs Control). (For interpretation of the references to colour in this figure legend, the reader is referred to the Web version of this article.)

2.8. Molecular docking

Molecular modelling studies were undertaken to provide further insights into the manner in which complex **1** first binds to the GRP78. Two possibilities were considered for the docking of the complex **1** with GRP 78: (i) Whether the complex **1** can bind to the ATPase domain of the GRP78 and, (ii) Whether the complex **1** can bind at the dimer interface utilizing the amino acid residue of both the monomer units (GRP78) of A and B. In the first scenario, it could not accommodate ATPase domain of GRP78 as the size of the complex **1** is large. In the second scenario, complex **1** was docked successfully into the dimer interface of GRP 78. The corresponding docking results are shown in Fig. 8 depicting the 3D diagram of the interaction of complex **1** with GRP78. From the protein ligand interaction (See Supplementary Figs. S5–S7), it is observed that Tyr 209 of both monomer units A and B make a strong H bond with distance 2.53 and 2.85 Å respectively. This seems to be the reason for the stability of the molecule (complex 1) within the binding pocket of the target protein GRP78. There are some electrostatic interactions with Glu 358 of both monomers A and B with distances 5.58 and 5.54 Å, respectively. In addition, Arg 214 of both monomer units also shows electrostatic interactions with distances 4.10 and 4.27 Å respectively. These electrostatic interactions are vital for the stabilization of the binding mode. Lys213 of unit A and Ile388 of unit B constitute a hydrophobic interaction with complex **1**, with distances 5.13 and 4.44 Å. Tyr 209 of unit B unit has a hydrophobic interaction with the distance 4.42 Å. The interactions between ligand (complex 1) and the hydrophobic side chains of protein (GRP78) contribute significantly to the binding free energy. The computer simulated docking results also support the results of biological activities of complex **1**.

2.9. In vivo anticancer activity of ruthenium(II) complex 1

In vivo chemotherapeutic potential of ruthenium(II) complex **1** against a CD133+HCT-116 CSCs derived tumor xenograft in athymic nude mice was investigated. Fig. 9A describes the protocol of the xenograft model. During the treatment period of two weeks, mice daily received 0.03 mg or 0.06 mg of complex **1**/kg body weight. Tumor weight and volume in the complex **1** treated mice group were significantly decreased as compared to the control group of mice (Fig. 9B and C). Tumor volume decreased 55% and 80% respectively in 0.03 and 0.06 mg/kg body weight treated animals compared to the control (Fig. 9D). Similarly, the observed tumor weight in control, low dose and high dose of the complex **1** treated animals are 3.2 g, 1.6 g, 1.15 g respectively, which shows the anticancer efficacy of complex **1** (Fig. 9E). Furthermore, the complex **1** treated mice group maintained normal body weight during the entire course of treatment and no mortalities were observed. These findings support the less toxic nature of complex **1** against normal cells. Treatment failure and tumor recurrence are mostly dependent on the CSCs population in cancer. In order to find the cytotoxic ability of complex **1** against CD133 + cells, mice were treated with anti-CD133 antibody tagged with alexaflour-705. The complex **1** treated experimental mice show a 2 fold and 4-fold reduction of

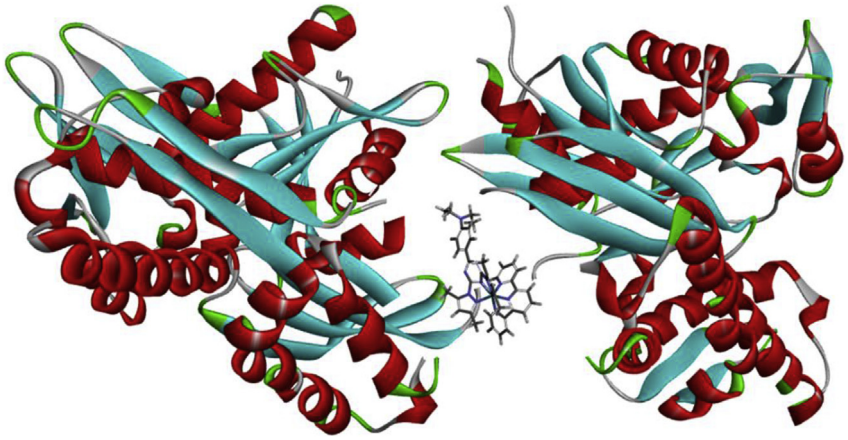

Fig. 8. The docking of complex **1** with dimeric GRP 78.

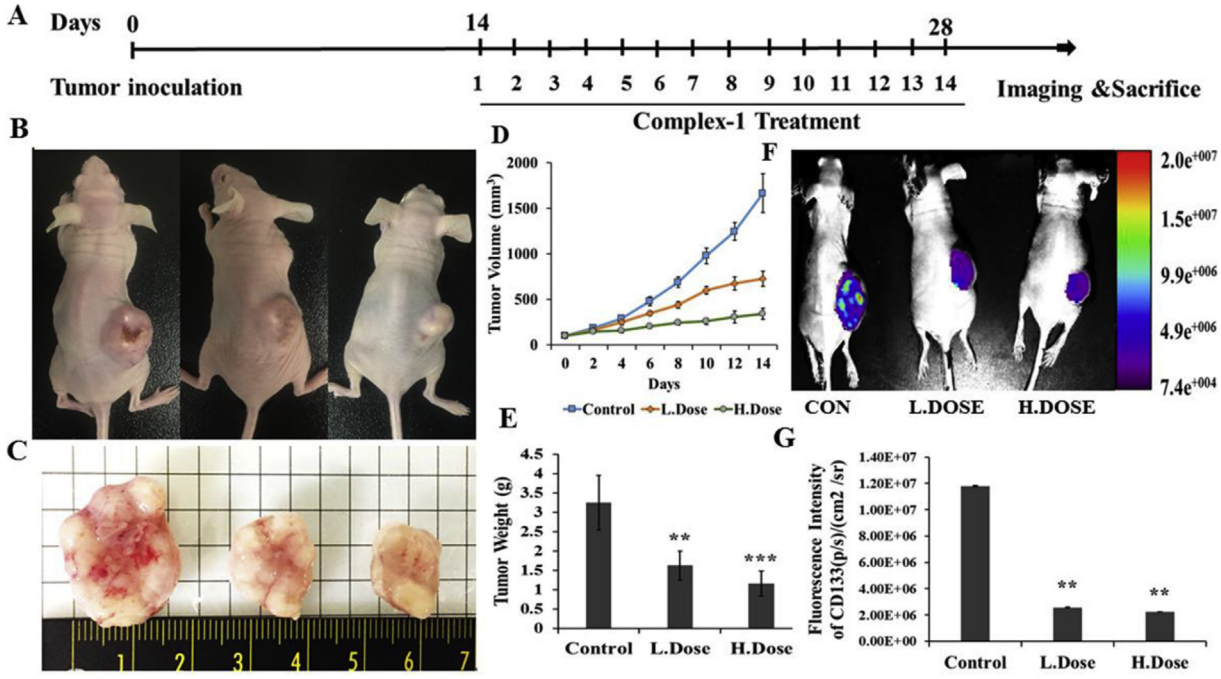

Fig. 9. (A) Treatment protocol. (B) Representative photographs of experimental mice (Control, Low dose, and High dose. (C) Representative photographs of tumor isolated from the experimental mice (Control, Low dose, and High dose). (D) Tumor volumes of experimental mice during treatment period. (E) Tumor weight of tumor xenograft isolated from the experimental mice. (F) Fluorescence emission of CD133 antibody tagged with Alexaflour680 in control and complex **1** treated experimental mice. (G) Bar graph represents the fluorescence intensity of CD133 antibody tagged with Alexaflour680.

fluorescence intensity respectively in the low and high dose treated groups, compared with control (Fig. 9G). This clearly indicates that the GRP78 suppressing nature of the complex **1** possesses the efficient cytotoxic ability against CSCs.

3. Conclusions

In summary, novel ruthenium(II) triazine complex **1** ($[Ru(bdpta)(tpy)]^{2+}$) was synthesized and characterized by spectroscopic methods. *In vitro* cytotoxicity study of complex **1** showed excellent IC_{50} value comparable to that previously reported for *cisplatin*. Interestingly, the complex **1**, with its excellent ROS generating potential and its tendency to accumulate in mitochondria and ER induces an intrinsic apoptosis in CSCs. Similarly, complex **1** causes MPTP, as well as MOMP in mitochondria, by elevating calcium and Bax/Bak respectively, which ensures the activation of caspase-3, an effector of apoptosis. Apart from this, direct interaction of complex **1** with the dimers of GRP-78 inflicts ROS mediated conformational changes to GRP-78, which leads to the ubiquitination of GRP-78. Degradation of GRP-78 is highly advantageous since elevated GRP78 is responsible for chemo and radio resistance. In addition, ruthenium(II) complex **1** exhibits excellent *in vivo* therapeutic potential against colon tumor xenograft. The observed results in this study show that complex **1** has the potential be a viable alternative to platinum based chemotherapeutic agents.

4. Experimental section

4.1. Materials and methods

Ruthenium trichloride trihydrate and other reagents or chemicals were purchased from Sigma Aldrich, South Korea. Analytical

grade solvents were purchased from Alfa Aesar or Sigma Aldrich South Korea, and degassed with 100% dry nitrogen for 20 min before use for the reactions. Deionized water was used for the preparation of sodium chlorate solution. For column purification acetonitrile and toluene commercial grade solvents were used and purchased from Daejung Chemicals, South Korea. ^{1}H and ^{13}C NMR spectra were recorded in deuterated methanol, chloroform or dimethyl sulfoxide (Cambridge Isotope Labs), containing 0.05% v/v TMS as an internal standard, using Bruker AVANCE400 and AVANCE600 spectrometer. The abbreviations for the peak multiplicities are as follows: s (singlet), d (doublet), dd (doublet of doublets), t (triplet), q (quartet), m (multiplet), and br (broad). Chemical shifts are reported in values (ppm) relative to internal TMS, and J values are reported in Hz. High resolution Mass spectroscopy data was obtained with an Agilent 6530 Q-TOF LC-MS spectrometer. MALDI-TOF mass spectrum was obtained with MALDI TOF-TOF 5800 System (AB SCIEX, USA). The column chromatography was carried out in Silica gel (Merck, silica gel 60, particle size 0.063–0.200 mm, 70–230 mesh ASTM) or neutral alumina (Alfa Aesar, 60 mesh, Brockmann grade 1, 58 A°) with mentioned commercial grade solvents as mobile phase. The progress of all reactions was monitored by thin layer chromatography (TLC), which was performed on $2.0 \times 4.0\ cm^2$ aluminum sheets precoated with silica gel 60 (HF-254, Merck) to a thickness of 0.25 mm. The developed chromatograms were viewed under ultraviolet light (254 and 365 nm). All the compounds including intermediates were detected with 254 nm UV light. Absorption spectra were recorded in 1 cm quartz cuvettes using Evolution™ 60 UV-Visible Spectrophotometer (Thermo Fischer Scientific, USA). Emission spectra were obtained on a Jasco-FP 6500 spectrofluorometer.

4.2. Synthesis and characteristics

4.2.1. Synthesis of ruthenium(II) complex 1: [Ru(bdpta)(tpy)](ClO$_4$)$_2$

The mixture of 2,2':6′,2″-terpyridine (**iii**) (300 mg, 1.29 mmol) and $RuCl_3 \cdot 3H_2O$ (0.336 g, 1.29 mmol) in anhydrous ethanol (80 ml) were refluxed at 80 °C for 3 h. The excess ethanol was concentrated by rotary evaporator to get the red solid which was washed with diethyl ether and hexane. The red solid of [Ru (tpy)Cl_3] was obtained and dried, it was used for the next step of the synthesis without further spectral analysis. 400 mg (0.85 mmol) of [Ru (tpy)Cl_3], 25 ml of dry ethylene glycol and 354 mg of **bdpta** ligand (0.9 mmol) were added and refluxed at 170 °C for 16 h under N_2 atmosphere. The reaction mixture was then cooled to room temperature and 1 M of $NaClO_4$ was added. The reddish brown solid was filtered and dissolved in dichloromethane. Dried over Na_2SO_4. Then the solvent was evaporated on the rotary evaporator. The crude ruthenium complex was purified twice by column chromatography on neutral alumina (CH_3CN/Toluene, 40/60, v/v). The dark reddish brown colour band was collected and sat. $NaClO_4$ was added, then the solvents were distilled to get product as perchlorate salt. The brown colour solid was then washed with diethyl ether, hexane and dried under vacuum. Yield: 400 mg, 51.4%. R_f value: 0.3 (CH_3OH: CH_2Cl_2, 20:80). ^{1}H NMR (400 MHz, CD_3OD) δ/ppm: 10.38–10.31 (m, 1H, tpy), 8.84 (dd, 1H, tpy), 8.69 (dd, J = 8.2, 1.4 Hz, 1H, tpy), 8.43–8.36 (m, 2H, aniline ring Ar proton), 8.35–8.25 (m, 2H, tpy), 7.98 (t, J = 7.9 Hz, 1H, tpy), 7.89 (ddd, J = 7.1, 5.7, 1.3 Hz, 1H, tpy), 7.66 (td, J = 7.7, 1.8 Hz, 1H, tpy), 7.20–7.10 (m, 2H, tpy), 6.97–6.89 (m, 2H, N,N-diethylaniline ring Ar proton), 6.52 (dd, J = 7.7, 1.1 Hz, 1H, tpy), 6.31 (s, 2H, pyrazole CH proton), 3.61 (q, J = 7.1 Hz, 4H, alkyl CH_2), 3.34 (s, 6H, pyrazole ring 2-CH_3), 3.07 (s, 6H, pyrazole ring 2-CH_3), 1.34–1.21 (m, 6H, alkyl -CH_3). ^{13}C NMR (600 MHz, DMSO-d_6): δ/ppm: 12.6 (pyrazole, -CH_3 carbon), 14.0 (N,N-diethylaniline group, -CH_3 carbon), 16.1 (N,N-diethylaniline group, -CH_2 carbon), 110.8 (tpy, CH), 111.4 (Pyrazole, -CH carbon), 121.0 (N,N-diethylaniline ring Ar CH), 121.2 (tpy, CH), 123.8 (tpy, CH), 131.6 (tpy, CH), 136.9 (N,N-diethylaniline ring Ar CH), 137.9 (tpy, CH), 144.0 (N,N-diethylaniline group, -C-N carbon), 149.2 (Pyrazole, -C=N carbon), 151.7 (tpy, C=N), 152.5 (Pyrazole, -C-N carbon), 155.4 (tpy, C-N) 156.3 (tpy, C=N), 164.0 (tpy, C-N), 164.2 (triazine C=N), 174.1 (triazine N=C-N). MALDI-TOF mass spectra: 752.07 ($C_{38}H_{39}N_{11}Ru$), HRMS (ESI): Calcd for $C_{38}H_{39}N_{11}Ru$: 750.8770, found: 750.8780. UV-Visible spectrum (CH_3CN): λ_{max} 396 nm and 515 nm.

4.3. Molecular docking

Molecular docking of complex **1** into the three-dimensional X-ray crystal structure of GRP78 (PDB: 3ldl) was carried out using Accelrys Discovery Studio (v 4.0) as implemented through the graphical user interface DS-CDOCKER protocol. The 3D structure of complex **1** was constructed using Discovery studio small molecule window and energy was minimized by CHARMm force field with and minimum RMS gradient of 0.09. The three-dimensional crystal structure of GRP78 (PDB: 3ldl) was retrieved from the RCSB Protein Data Bank (http://www.rcsb.org/pdb/). Discovery studio 4.0 uses a simulated annealing procedure to explore the binding possibilities of a ligand in a binding pocket. Before the docking procedure, all bound water molecules and ATP molecules as heteroatoms were removed from the protein crystal structure. The homodimer structure of GRP 78 was taken to dock the drug molecule (complex 1). Binding site uses a CHARMm-based molecular dynamics scheme to seek for the optimal binding sites for docking. Then, the optimal binding site was chosen based on the shape and location of the cavity, the location of the residue and the conserved amino acid. Among the nine potential binding sites, the site 1 was chosen for docking study. A site sphere radius was set to assign the entire binding pocket where the other parameters were set as default. The docking program CDOCKER was used to perform the automated molecular simulation where the Top hits was set as 10, the Random Conformations was set as 10. The top compounds were ranked by the corresponding values of -CDOCKER energy, -CDOCKER interaction energy and all the values were preserved to find the most probable binding mode.

4.4. Maintenance of cell culture

Breast cancer cell line MCF-7 and colon cancer cell line HCT-116 was obtained from the Korean Cell Line Bank (KCLB, Seoul, Korea). Dulbecco's modified Eagle's medium (DMEM; Gibco-BRL, Grand Island, NY) supplemented with 10% heat-inactivated fetal bovine serum (FBS; GibcoBRL, Grand Island, NY), 10 μg/mL streptomycin, 100 U/mL penicillin, and 5 μg/mL neomycin (PSN; 15,640–055, Gibco-BRL) was used to culture both MCF-7 and HCT-116 cell line. Cell cultures were maintained at 37 °C in a humidified atmosphere containing 5% CO_2.

4.5. Isolation of CSC from the MCF-7 and HCT-116 cell line

Cancer stem cell marker CD44 was used to sort out CSC from MCF-7 cell line. Similarly, CD133 marker was used to isolate CSC from HCT-116 cell line. CSCs from cell lines were sorted by using CD44 and CD133 microbead kit (MACS Miltenyi Biotec) as described previously [67]. Briefly, MCF-7 and HCT-116 cells were detached from the cell culture by using Accutase cell dissociation reagent. Cells were centrifuged at 230 rcf for 3 min and supernatant was discorded. Then, cells were resuspended in a mixture containing 80 μL of sorting buffer and 20 μL of microbead solution provided in the kit and incubated for 15 min at 4 °C. Followed by the incubation,

cells were dissolved in 1 ml of sorting buffer and centrifuged (300 g, 10 min) to collect the cell pellet. The cell pellet was again resuspended in 500 μL of sorting buffer. The LS column and pre-separation filter provided in the kit (MACS Miltenyi Biotec) were fixed in the magnetic field of the MACS separator and subsequently rinsed with cell sorting buffer. The prepared cell suspension was pipetted into pre-separation filter. CSCs bound with magnetic beads were strongly adhered with LS column, the unbound cells were flushed out by the repeated application of sorting buffer. Finally, the CSC adhered with LS column were flushed out by applying a pressure using syringe provided in the kit.

4.6. Cellular uptake

The cellular uptake in CD44+MCF-7 cells was monitored by FACS analysis at different time point. CD44+MCF-7 cells were treated with complex **1** at 20, 40, and 60 min. After incubation, fluorescence intensity of complex **1** was analysed by using FACS. Cells were excited with 488 nm laser and then emission was observed at 515–545 nm range. For each sample, approximately 10,000 cells were measured. Data was analysed using FlowJo software.

4.7. Cytotoxicity assay in vitro

Sulforhodamine B based cytotoxicity assay was performed according to the manufacturer's protocol (In Vitro Toxicology Assay Kit, Sigma-Aldrich, USA). Briefly, 1×10^6 cells were separately seeded in 24 well plate and incubated at 37 °C in DMEM medium supplemented with 10% FBS for 48 h. Afterward, cells were treated with Ru(II) complex **1** at different concentrations (0–100 μM) and incubated for 48 h. After treatment, cells were fixed using ice cold trichloroacetic acid (50%, w/v) and incubated for 1 h at 4 °C. The fixing solution was removed and plates were washed with water and air dried. 0.4% Sulforhodamine B Solution was added to the culture wells and incubated for 20 min at room temperature. After staining, culture wells were washed with 1% acetic acid and air dried. Bound SRB was eluted with 10 mM Tris. Absorbance was read at a wavelength of 540. The background absorbance of multiwell plates were measured at 690 nm and subtract from the measurement at 565 nm. Experiments were performed in triplicate.

4.8. Quantification of intracellular ROS

Cancer stem cells of MCF-7 and HCT-116 were seeded in 12-well culture plate and incubated overnight at 37 °C in 5% CO_2. Then, cells were treated with and without complex **1** for 6 h and incubated at 37 °C in 5% CO_2 environment. At the end of treatment, cells were fixed with 4% formaldehyde and incubated at room temperature for 10 min. After washing with 1 × PBS, cells were treated with 20 μM of 2′,7′-dichlorofluorescin diacetate (DCFDA) and incubated for 15 min at room temperature. Fluorescence intensity of ROS induced 2′,7′-dichlorofluorescin was measured with the excitation and emission wavelengths of 495 and 529 nm.

4.9. Intracellular localization assay

CSCs were seeded on cover glass and incubated at 37 °C for 24 h. Then, cells were treated with 10 μM of ruthenium complex and incubated for 2 h at 37 °C. After drug treatment, cells were washed with 1 × PBS and incubated with either MitoTracker® Red CMXRos (Thermofischer scientific, USA) or ER-ID® Red (Enzo Life Sciences, Inc., USA) along with Hoechst 33258 nuclear dye (Sigma Aldrich, USA) for 30 min. Finally, cells were fixed with 4% formaldehyde for 15 min at room temperature. Fluorescence intensity of tracker dyes and ruthenium complexes were observed using Confocal Microscope (Leica, TCS SP8). Complex **1** was excited at 514 nm and emission was measured at 540–600 nm. MitoTracker Red CMXRos and ER-ID® Red dye was excited at 594 nm and emission was observed at 605–700 nm. Excitation and emission wavelength of Hoechst 33258 nuclear dye was 405 nm and 450–500 nm.

4.10. High-content MPT, cytosolic Ca^{2+} and caspase3/7 screening assay

CSCs were cultured in 12 well culture flask and maintained in DMEM medium supplemented with 10% FBS for 24 h at 37 °C in 5% CO_2 atmosphere. Then, cells were maintained with and without complex **1** for 16 h. After washing with 1 × PBS buffer, cells were incubated with calcium indicator orange (Invitrogen, CA, and USA) at room temperature in the dark for 45 min. Cells were washed with 1 × PBS and incubated with calceinacetoxymethyl ester (Calcein-AM) (Invitrogen, CA, USA) for 30 min at 37 °C. Then, caspase-3 substrate (Thermo Scientific, U.S.A) was added, and cells were incubated at 37 °C in the dark for 6 min. Followed by $CoCl_2$ was added and incubated at 37 °C in the dark for 10 min. Finally, cells were washed with 1 × PBS and subjected to imaging analysis using acousto-optic tunable filter (AOTF) enabled microscopic device as described previously [56]. Calcium indicator orange was excited at 561 nm and emission was measured at 549 nm. Excitation and emission of Calcein-AM was 488 nm and 516 nm, respectively. Caspase-3 was excited at 488 nm and emission was measured at 530 nm. Images were analysed using commercially available software (MetaMorph, Version 7.7, Molecular Devices, CA, and USA).

4.11. List of antibodies

The following antibodies were used for western blot and immunofluorescence analysis: Total cell lysates were collected using RIPA sample buffer. Western blot analysis was performed as described previously. The following antibodies were used: Goat anti-GRP78 (Cat. No. sc-1051), mouse anti-Bax (Cat. No. sc-23959) and Bcl-2 (Cat. No. sc-7382) antibodies; and rabbit anti-Bak (Cat. No. sc-832) were purchased from Santa Cruz Biotechnology (Santa Cruz, CA, USA). HRP- conjugated goat anti-mouse (Cat. No. sc-2005), HRP conjugated anti-rabbit IgG (Cat. No. sc-2030), PE-conjugated goat anti-mouse IgG (Cat. No. sc-3738), FITC conjugated anti-rabbit IgG (Cat. No. sc-2012), and FITC-conjugated anti-goat IgG (Cat. No. sc-2024) were purchased from Santa Cruz Biotechnology (Santa Cruz, CA, USA), and HRP-conjugated anti-goat IgG (Cat. No. ab-97110) was purchased from abcam (abcam, USA).

4.12. Western blot analysis

Total cell lysates were collected using RIPA buffer. After centrifuging at 12000 rpm for 15min, the supernatants were collected. The protein samples were separated on a 10% SDS-PAGE and transferred to a nitrocellulose membrane. The membrane was blocked in 5% skim milk in TBS-T for 1 h. After blocking, the membranes were incubated with the primary antibodies specific for Bax (1:1000), Bak (1:1000), Bcl-2 (1:2000), and GRP-78 (1:500) in TBS-T for 1 h. After washing twice with TBS-T for 10 min, the membrane was incubated with an appropriate HRP conjugated secondary antibody. The membranes were then developed with an enhanced chemiluminescence reagent (Thermo Scientific, U.S.A).

4.13. Plasmid construction and transfection of GRP78, CLU and ATR

Genomic DNA from the control human sample was isolated using a QIAamp DNA Blood Mini Kit (Qiagen, Valencia, CA) as

instructed by the manufacturer. DNA (200 ng) was amplified with the specific primers, GRP78: Forward (50 pmol; 5′-AAAGCTTTTAT-GAAGCTCTCCCTGGTGG-3′) and GRP78:Reverse (50 pmol; 5′-AGGATCCCTACAACTCATCTTTTTCTGCTG-3′) or CLU: Forward (50 pmol; 5′-AAAGCTTATGCAGGTTTGCAGCCAGC-3′) and Clu: Reverse (50 pmol; 5′- GGATCCCTCCTCCCGGTGCTTTTTG-3′), or ATR: Forward (50 pmol; 5′- AAGCTTATGGCCACGGCGGAGC-3′) and ATR: Reverse (50 pmol; 5′- GGATCCTTTTATTTTATTTTCCTCACTCTCCT -3′), with the following temperature profile: 95 °C for 4 min; 30 cycles of 95 °C for 30 s, 59–66 °C for 30 s and 72 °C for 1 min; and a final extension at 72 °C for 5 min. GRP78, CLU and ATR primers were designed to amplify GRP78, CLU and ATR transcripts of the respective genes. PCR amplification was confirmed by analysis of the amplified 1.9 kb GRP78, 1.5 kb CLU and 850 bp ATR fragments using 1.2% agarose gel with standard molecular weight markers. PCR-amplified GRP78, CLU and ATR fragments were restricted with HindIII/BamHI enzymes. Restricted GRP78, CLU and ATR fragments were ligated with pTag-YFP-C (4.7 kb; Evrogen, Moscow, Russia), pDs-Red2-N1 (4.7 kb; Clontech, USA) and pAC-GFP1-N1 (4.7 kb; Clontech, USA), respectively. Ligated fusion gene vectors were separately transformed into competent *E. coli* DH5a cells through chemical transformation as suggested by the manufacturer (Invitrogen, Carlsbad, CA). The transformants (pTag-YFP-GRP78-C, pDs-CLU-Red2-N1 and pAC-ATR-GFP1-N1) were selected on LB agar plates supplemented with kanamycin (30 μg/mL). Plasmids from resistant colonies were isolated using a Plasmid Midi Kit (Qiagen). Plasmids cloned with GRP78, CLU and ATR genes were cotransfected into HEK-293 cells. Human embryonic kidney cells (HEK-293) were obtained from the Korean Cell Line Bank (KCLB1, Seoul, South Korea) and cultured in DMEM supplemented with 10% FBS. First, HEK-293 cells (5×10^5 cells per well) were seeded into 24-well culture plates containing DMEM and FBS without antibiotics for up to 24 h. Next day, the plasmids DNA (GRP78, CLU and ATR) were co-transfected into HEK-293 cells using Lipofectamine 2000 (Invitrogen) according to the manufacturer's directions. The cell culture plates were kept at 37 °C in a CO_2 incubator for 6 h. The cells were then washed and grown in the complete medium for 48 h at 37 °C in a CO_2 incubator. Followed by, GRP78, CLU and ATR amplified cells were incubated with different concentrations of complex **1** for 16 h at 37 °C in a 5% CO_2 incubator. Fluorescence micrographs of HEK-293 cells were then taken for quantitative analysis. Data acquisition and quantitative analysis were performed as previously described [68].

4.14. Quantitative RT–PCR

HEK293 cells were treated with and without complex **1** for 16 h and maintained in DMEM medium at 37 °C in a CO_2 incubator. Afterward, total RNA was extracted as described by the manufacturer's protocol (Dynabeads® MRNA Purification Kit, Invitrogen, USA). Integrity of isolated RNA was qualitatively assessed by the ratio of absorbance at 260/280 nm and then by 1% agarose RNA gel electrophoresis. The concentration of RNA was measured at 260 nm using a Nanodrop (Thermo Scientific, U.S.A). From the total RNA, cDNA specific for GAPDH, and GRP78 were prepared using QuantiTect Reverse Transcription Kit (Qiagen, USA) as described by the manufacturer's protocol. Two picomol of primers were used for the amplification of target m-RNA. Starting template quantity of the samples was determined using GAPDH expression, and then quantitative PCR reactions were carried out. The following primers were used, GAPDH sense CATGAGAAGTATGACAACAGCCT, antisense AGTCCTTCCACGATACCAAAGT; GRP78 sense GTTCTTGCCGTTCA AGGTGG, antisense TGGTACAGTAACAACTGCATG. SYBR green method was adopted to perform the RT-PCR (SYBR green qPCR kit, Thermo Scientific, USA). Applied Biosystems™ Real-Time PCR instrument (7300) was used to execute the RT- PCR. Data were normalized with GAPDH and analysed by the 2−ΔΔCT method.

4.15. Conjugation of GRP-78 with quantum dot-antibody for immunofluorescence assay

The antibody specific for GRP78 was conjugated with Q-dot 705 (Quantum Dot Conjugation Kit; Invitrogen, Carlsbad, CA, USA), respectively. To initiate the Q-dot conjugation with antibody, Firstly, the antibodies were treated with dithiothreitol (DTT) which introduce disulphide bond break and convert the antibodies into reduced state. Then, antibodies were incubated with maleimide-functionalized Q-dot for 1 h at room temperature. Then, the conjugations were treated with 2-mercaptoethanol in order to remove the maleimide group. The unconjugated Q-dot were eluted using column provided in the kit. The Q-dot -antibody conjugation was diluted at 1:200 with 1% BSA for immunofluorescence analysis. The excitation and emission used for the fluorescence analysis was 405/705 respectively.

4.16. Immunofluorescence staining and confocal microscopy

Immunofluorescence analysis for Bcl-2, Bax, Bak, and Q-dot-conjugated GRP78 (Q-dot GRP-78) was performed as described previously [69,70]. Briefly, Cells cultured on cover slides were subjected to complex 1 treatment and then fixed with 4% formaldehyde for 15 min. After fixation, cells were washed with 1X PBS and incubated with primary antibodies (Bax and Bak, 1:150; GRP-78, 1:200) for 1 h. After washing with 1XTBS, Bax and Bak treated cells were incubated with PE-conjugated goat anti-mouse IgG (1:250) for 1 h. The cell nuclei were stained with Hoechst DNA stain (1:2000) for 5 min. After washing with TBS, cells were imaged using fluorescence microscopy. The excitation and emission used for the fluorescence analysis of PE-conjugated secondary antibody was 561nm/575–620 nm respectively. The excitation and emission maximum for Q-dot GRP-78 was 405/705 respectively. Fluorescence images were obtained using an Olympus FLUOVIEW 500 confocal microscope.

4.17. Human colon carcinoma xenograft model

In vivo animal experiments were carried out according to the protocols approved by the institutional animal care and use committee of Seoul National University. Seven-week old Swiss female athymic mice were purchased from Daehan Biolink (Seoul, Korea). All Mice were housed in a specific pathogen-free condition at the animal facility centre of the College of Pharmacy at Seoul National University (Seoul, Korea) and were maintained at 25 °C with a 12 h light and dark cycle. CD133+HCT-116 cells (3×10^6 Cells) isolated from HCT-116 cell culture were mixed with 100 μL of LDEV-Free Reduced Growth Factor Basement Membrane Matrix (Geltrex; Thermofischer Scientific, USA) and then subcutaneously injected in the right flank of the mice. When tumor reached the volume of 100 mm^3, the mice were divided in to three groups. Each group contains six animal. Control group received intraperitoneal (i.p.) injection of 1xPBS containing 4% DMSO. Other two group of mice were treated daily with 0.03 mg/kg/body weight or 0.06 mg/kg/body weight of complex **1** by i. p. injection. Treatment was repeated for 2 weeks and stopped when control tumor size reached approximately 1500 mm^3. Mice were monitored daily for tumor size and body weight during the course of treatment. Tumor volumes (mm^3) were calculated as follows: volume = (largest diameter in mm) (perpendicular diameter in mm)$^2 \times 0.5$.

4.18. Optical imaging of CD133 in tumor xenograft

Tumor treatment was stopped when the control tumor size reached 1000 mm^3. Afterward, mice were intravenously injected with 50 mg of Alexa flour 705 tagged anti-CD133 antibody. Four hours post injection, mice were anesthetized with isoflurane. Fluorescence images of CD133 in control and complex **1** treated mice were taken by an optical tomography system. Mice were placed on the imaging platform and images were taken using the Optix *in vivo* imaging system (Optix MX3, ART Advanced Research Technologies INC, Canada).

4.19. Statistical analysis

All experiments were repeated three times within three independent cultures ($n = 3$). The results are expressed as mean ± SD. Data was compared using one-way analysis of variance (ANOVA) with a Tukey–Kramer post-test. The results were considered to be statistically significant when $p \leq 0.05$.

Acknowledgments

This work was supported by National Research Foundation of Korea (NRF) grant funded by the Ministry of Education, Science and Technology (MEST) (2016R1A4A1010796). We are grateful to the Research Institute of Pharmaceutical Sciences at Seoul National University for providing experimental equipment's, in-vitro and animal facility.

Appendix A. Supplementary data

Supplementary data related to this article can be found at https://doi.org/10.1016/j.ejmech.2018.07.048.

References

[1] S. Dasari, P.B. Tchounwou, Cisplatin in cancer therapy: molecular mechanisms of action, Eur. J. Pharmacol. 740 (2014) 364–378.
[2] B. Stordal, N. Pavlakis, R. Davey, Oxaliplatin for the treatment of cisplatin-resistant cancer: a systematic review, Canc. Treat Rev. 33 (2007) 347–357.
[3] L. Galluzzi, L. Senovilla, I. Vitale, J. Michels, I. Martins, O. Kepp, M. Castedo, G. Kroemer, Molecular mechanisms of cisplatin resistance, Oncogene 31 (2012) 1869–1883.
[4] D.-W. Shen, L.M. Pouliot, M.D. Hall, M.M. Gottesman, Cisplatin resistance: a cellular self-defense mechanism resulting from multiple epigenetic and genetic changes, Pharmacol. Rev. 64 (2012) 706–721.
[5] L. Galluzzi, I. Vitale, J. Michels, C. Brenner, G. Szabadkai, A. Harel-Bellan, M. Castedo, G. Kroemer, Systems biology of cisplatin resistance: past, present and future, Cell Death & Disease 5 (2014) e1257.
[6] F. Lentz, A. Drescher, A. Lindauer, M. Henke, R.A. Hilger, C.G. Hartinger, M.E. Scheulen, C. Dittrich, B.K. Keppler, U. Jaehde, Pharmacokinetics of a novel anticancer ruthenium complex (KP1019, FFC14A) in a phase I dose-escalation study, Anti Canc. Drugs 20 (2009) 97–103.
[7] R. Trondl, P. Heffeter, C.R. Kowol, M.A. Jakupec, W. Berger, B.K. Keppler, NKP-1339, the first ruthenium-based anticancer drug on the edge to clinical application, Chem. Sci. 5 (2014) 2925–2932.
[8] L. Chen, G. Li, F. Peng, X. Jie, G. Dongye, K. Cai, R. Feng, B. Li, Q. Zeng, K. Lun, The induction of autophagy against mitochondria-mediated apoptosis in lung cancer cells by a ruthenium (II) imidazole complex, Oncotarget 7 (2016) 80716.
[9] L. Gu, X. Li, Q. Ran, C. Kang, C. Lee, J. Shen, Antimetastatic activity of novel ruthenium (III) pyridine complexes, Cancer Med. 5 (2016) 2850–2860.
[10] V. Pierroz, T. Joshi, A. Leonidova, C. Mari, J. Schur, I. Ott, L. Spiccia, S. Ferrari, G. Gasser, Molecular and cellular characterization of the biological effects of ruthenium (II) complexes incorporating 2-pyridyl-2-pyrimidine-4-carboxylic acid, J. Am. Chem. Soc. 134 (2012) 20376–20387.
[11] A. Weiss, R.H. Berndsen, M. Dubois, C. Müller, R. Schibli, A.W. Griffioen, P.J. Dyson, P. Nowak-Sliwinska, In vivo anti-tumor activity of the organometallic ruthenium (ii)-arene complex [Ru (η 6-p-cymene) Cl $_2$ (pta)](RAPTA-C) in human ovarian and colorectal carcinomas, Chem. Sci. 5 (2014) 4742–4748.
[12] M.V. Babak, S.M. Meier, K.V. Huber, J. Reynisson, A.A. Legin, M.A. Jakupec, A. Roller, A. Stukalov, M. Gridling, K.L. Bennett, Target profiling of an antimetastatic RAPTA agent by chemical proteomics: relevance to the mode of action, Chem. Sci. 6 (2015) 2449–2456.
[13] M. Pal, U. Nandi, D. Mukherjee, Detailed account on activation mechanisms of ruthenium coordination complexes and their role as antineoplastic agents, Eur. J. Med. Chem. 150 (2018) 419–445.
[14] D. Wan, B. Tang, Y.-J. Wang, B.-H. Guo, H. Yin, Q.-Y. Yi, Y.-J. Liu, Synthesis and anticancer properties of ruthenium (II) complexes as potent apoptosis inducers through mitochondrial disruption, Eur. J. Med. Chem. 139 (2017) 180–190.
[15] A. Bijelic, S. Theiner, B.K. Keppler, A. Rompel, X-ray structure analysis of indazolium trans-[Tetrachlorobis (1 H-indazole) ruthenate (III)](KP1019) bound to human serum albumin reveals two ruthenium binding sites and provides insights into the drug binding mechanism, J. Med. Chem. 59 (2016) 5894–5903.
[16] M. Groessl, M. Terenghi, A. Casini, L. Elviri, R. Lobinski, P.J. Dyson, Reactivity of anticancer metallodrugs with serum proteins: new insights from size exclusion chromatography-ICP-MS and ESI-MS, J. Anal. Atomic Spectrom. 25 (2010) 305–313.
[17] K. Śpiewak, G. Stochel, M. Brindell, Influence of redox activation of NAMI-A on affinity to serum proteins: transferrin and albumin, J. Coord. Chem. 68 (2015) 3181–3192.
[18] J.C. Kwok, D.R. Richardson, The iron metabolism of neoplastic cells: alterations that facilitate proliferation? Crit. Rev. Oncol.-Hematol. 42 (2002) 65–78.
[19] M.J. Brookes, S. Hughes, F.E. Turner, G. Reynolds, N. Sharma, T. Ismail, G. Berx, A.T. McKie, N. Hotchin, G.J. Anderson, Modulation of iron transport proteins in human colorectal carcinogenesis, Gut 55 (2006) 1449–1460.
[20] S. Leijen, S.A. Burgers, P. Baas, D. Pluim, M. Tibben, E. van Werkhoven, E. Alessio, G. Sava, J.H. Beijnen, J.H. Schellens, Phase I/II study with ruthenium compound NAMI-A and gemcitabine in patients with non-small cell lung cancer after first line therapy, Invest. N. Drugs 33 (2015) 201–214.
[21] E. Alessio, Thirty years of the drug candidate NAMI-a and the myths in the field of ruthenium anticancer compounds: a personal perspective, Eur. J. Inorg. Chem. 2017 (2017) 1549–1560.
[22] P. Singla, V. Luxami, K. Paul, Triazine–benzimidazole hybrids: anticancer activity, DNA interaction and dihydrofolate reductase inhibitors, Bioorg. Med. Chem. 23 (2015) 1691–1700.
[23] M.E. Van Dort, H. Hong, H. Wang, C.A. Nino, R.L. Lombardi, A.E. Blanks, S. Galbán, B.D. Ross, Discovery of bifunctional oncogenic target inhibitors against allosteric mitogen-activated protein kinase (MEK1) and phosphatidylinositol 3-kinase (PI3K), J. Med. Chem. 59 (2016) 2512–2522.
[24] P. Dao, N. Smith, C.I. Tomkiewicz-Raulet, E.d. Yen-Pon, M. Camacho-Artacho, D. Lietha, J.-P. Herbeuval, X. Coumoul, C. Garbay, H. Chen, Design, synthesis, and evaluation of novel imidazo [1, 2-a][1, 3, 5] triazines and their derivatives as focal adhesion kinase inhibitors with antitumor activity, J. Med. Chem. 58 (2014) 237–251.
[25] M.I. Polson, E.A. Medlycott, G.S. Hanan, L. Mikelsons, N.J. Taylor, M. Watanabe, Y. Tanaka, F. Loiseau, R. Passalacqua, S. Campagna, Ruthenium Complexes of Easily Accessible Tridentate Ligands Based on the 2-Aryl-4, 6-bis (2-pyridyl)-s-triazine Motif: absorption Spectra, Luminescence Properties, and Redox Behavior, Chem. Eur J. 10 (2004) 3640–3648.
[26] E.A. Medlycott, G.S. Hanan, F. Loiseau, S. Campagna, Tuning the excited-state energy of the organic chromophore in bichromophoric systems based on the Ru(II) complexes of tridentate ligands, Chem. Eur J. 13 (2007) 2837–2846.
[27] J. Liu, Y. Chen, G. Li, P. Zhang, C. Jin, L. Zeng, L. Ji, H. Chao, Ruthenium (II) polypyridyl complexes as mitochondria-targeted two-photon photodynamic anticancer agents, Biomaterials 56 (2015) 140–153.
[28] M.P. Barr, S.G. Gray, A.C. Hoffmann, R.A. Hilger, J. Thomale, J.D. O'Flaherty, D.A. Fennell, D. Richard, J.J. O'Leary, K.J. O'Byrne, Generation and characterisation of cisplatin-resistant non-small cell lung cancer cell lines displaying a stem-like signature, PLoS One 8 (2013), e54193.
[29] A. Flemming, Cancer stem cells: targeting the root of cancer relapse, Nat. Rev. Drug Discov. 14 (2015) 165.
[30] B.S. Berlett, E.R. Stadtman, Protein oxidation in aging, disease, and oxidative stress, J. Biol. Chem. 272 (1997) 20313–20316.
[31] E.R. Stadtman, Protein oxidation and aging, Free Radical Research 40 (2006) 1250–1258.
[32] T. Kosakowska-Cholody, J. Lin, S. Srideshikan, L. Scheffer, N. Tarasova, J. Acharya, HKH40A downregulates GRP78/BiP expression in cancer cells, Cell Death & Disease 5 (2014) e1240.
[33] L. Zhang, S. Wang, Wangtao, Y. Wang, J. Wang, L. Jiang, S. Li, X. Hu, Q. Wang, Upregulation of GRP78 and GRP94 and its function in chemotherapy resistance to VP-16 in human lung cancer cell line SK-MES-1, Canc. Invest. 27 (2009) 453–458.
[34] N. Al Nakouzi, C.K. Wang, E. Beraldi, W. Jager, S. Ettinger, L. Fazli, L. Nappi, J. Bishop, F. Zhang, A. Chauchereau, Clusterin knockdown sensitizes prostate cancer cells to taxane by modulating mitosis, EMBO Molecular Medicine (2016), e201506059.
[35] C. Hoeller, B. Pratscher, C. Thallinger, D. Winter, D. Fink, B. Kovacic, V. Sexl, V. Wacheck, M.E. Gleave, H. Pehamberger, Clusterin regulates drug-resistance in melanoma cells, J. Invest. Dermatol. 124 (2005) 1300–1307.
[36] M. Kawasumi, B. Lemos, J.E. Bradner, R. Thibodeau, Y.-s. Kim, M. Schmidt, E. Higgins, S.-w. Koo, A. Angle-Zahn, A. Chen, Protection from UV-induced skin carcinogenesis by genetic inhibition of the ataxia telangiectasia and Rad3-related (ATR) kinase, Proc. Natl. Acad. Sci. Unit. States Am. 108 (2011) 13716–13721.
[37] C. Yang, L.M. Fu, Y. Wang, J.P. Zhang, W.T. Wong, X.C. Ai, Y.F. Qiao, B.S. Zou, L.L. Gui, A highly luminescent europium complex showing visible-light-

sensitized red emission: direct observation of the singlet pathway, Angew. Chem. 116 (2004) 5120–5123.
[38] V.S. Padalkar, V.S. Patil, N. Sekar, Synthesis and photo-physical properties of fluorescent 1, 3, 5-triazine styryl derivatives, Chem. Cent. J. 5 (2011) 77.
[39] S. Ding, C. Li, N. Cheng, X. Cui, X. Xu, G. Zhou, Redox regulation in cancer stem cells, Oxidative Med. Cell. Longev. 2015 (2015).
[40] O. Herault, K.J. Hope, E. Deneault, N. Mayotte, J. Chagraoui, B.T. Wilhelm, S. Cellot, M. Sauvageau, M.A. Andrade-Navarro, J. Hébert, A role for GPx3 in activity of normal and leukemia stem cells, J. Exp. Med. 209 (2012) 895–901.
[41] S.J. Dougan, A. Habtemariam, S.E. McHale, S. Parsons, P.J. Sadler, Catalytic organometallic anticancer complexes, Proc. Natl. Acad. Sci. Unit. States Am. 105 (2008) 11628–11633.
[42] E.B. Kurutas, The importance of antioxidants which play the role in cellular response against oxidative/nitrosative stress: current state, Nutr. J. 15 (2016) 71.
[43] P.T. Schumacker, Reactive oxygen species in cancer: a dance with the devil, Canc. Cell 27 (2015) 156–157.
[44] E. Panieri, M. Santoro, ROS homeostasis and metabolism: a dangerous liason in cancer cells, Cell Death & Disease 7 (2016) e2253.
[45] S. Prasad, S.C. Gupta, A.K. Tyagi, Reactive oxygen species (ROS) and cancer: role of antioxidative nutraceuticals, Canc. Lett. 387 (2017) 95–105.
[46] D. Trachootham, J. Alexandre, P. Huang, Targeting cancer cells by ROS-mediated mechanisms: a radical therapeutic approach? Nat. Rev. Drug Discov. 8 (2009) 579–591.
[47] O. Nagano, S. Okazaki, H. Saya, Redox regulation in stem-like cancer cells by CD44 variant isoforms, Oncogene 32 (2013) 5191–5198.
[48] A.T. Dharmaraja, Role of reactive oxygen species (ROS) in therapeutics and drug resistance in cancer and bacteria, J. Med. Chem. 60 (2017) 3221–3240.
[49] A. Sznarkowska, A. Kostecka, K. Meller, K.P. Bielawski, Inhibition of cancer antioxidant defense by natural compounds, Oncotarget 8 (2017) 15996.
[50] J. Chen, F. Peng, Y. Zhang, B. Li, J. She, X. Jie, Z. Zou, M. Chen, L. Chen, Synthesis, characterization, cellular uptake and apoptosis-inducing properties of two highly cytotoxic cyclometalated ruthenium (II) β-carboline complexes, Eur. J. Med. Chem. 140 (2017) 104–117.
[51] D. Mekahli, G. Bultynck, J.B. Parys, H. De Smedt, L. Missiaen, Endoplasmic-reticulum calcium depletion and disease, Cold Spring Harbor Perspect. Biol. 3 (2011) a004317.
[52] G.G. Johnson, M.C. White, J.-H. Wu, M. Vallejo, M. Grimaldi, The deadly connection between endoplasmic reticulum, Ca2+, protein synthesis, and the endoplasmic reticulum stress response in malignant glioma cells, Neuro Oncol. 16 (2014) 1086–1099.
[53] B. Bhandary, A. Marahatta, H.-R. Kim, H.-J. Chae, An involvement of oxidative stress in endoplasmic reticulum stress and its associated diseases, Int. J. Mol. Sci. 14 (2012) 434–456.
[54] M.P. Mattson, S.L. Chan, Calcium orchestrates apoptosis, Nat. Cell Biol. 5 (2003) 1041–1043.
[55] R.N. Kitsis, J.D. Molkentin, Apoptotic cell death "Nixed" by an ER–mitochondrial necrotic pathway, Proc. Natl. Acad. Sci. Unit. States Am. 107 (2010) 9031–9032.
[56] S. Rangasamy, H. Ju, S. Um, D.-C. Oh, J.M. Song, Mitochondria and DNA targeting of 5, 10, 15, 20-tetrakis (7-sulfonatobenzo [b] thiophene) porphyrin-induced photodynamic therapy via intrinsic and extrinsic apoptotic cell death, J. Med. Chem. 58 (2015) 6864–6874.
[57] Y. Kushnareva, A.Y. Andreyev, T. Kuwana, D.D. Newmeyer, Bax activation initiates the assembly of a multimeric catalyst that facilitates Bax pore formation in mitochondrial outer membranes, PLoS Biol. 10 (2012), e1001394.
[58] L. Große, C.A. Wurm, C. Brüser, D. Neumann, D.C. Jans, S. Jakobs, Bax assembles into large ring-like structures remodeling the mitochondrial outer membrane in apoptosis, EMBO J. 35 (2016) 402–413.
[59] F. Ciardiello, G. Tortora, Inhibition of bcl-2 as cancer therapy, Ann Oncol. 13 (2002) 501–502.
[60] N.N. Danial, BCL-2 family proteins: critical checkpoints of apoptotic cell death, Clin. Canc. Res. 13 (2007) 7254–7263.
[61] M. Chami, A. Prandini, M. Campanella, P. Pinton, G. Szabadkai, J.C. Reed, R. Rizzuto, Bcl-2 and Bax exert opposing effects on Ca2+ signaling, which do not depend on their putative pore-forming region, J. Biol. Chem. 279 (2004) 54581–54589.
[62] L. Scorrano, S.A. Oakes, J.T. Opferman, E.H. Cheng, M.D. Sorcinelli, T. Pozzan, S.J. Korsmeyer, BAX and BAK regulation of endoplasmic reticulum Ca2+: a control point for apoptosis, Science 300 (2003) 135–139.
[63] W.-X. Zong, C. Li, G. Hatzivassiliou, T. Lindsten, Q.-C. Yu, J. Yuan, C.B. Thompson, Bax and Bak can localize to the endoplasmic reticulum to initiate apoptosis, J. Cell Biol. 162 (2003) 59–69.
[64] A. Ruiz-Vela, J.T. Opferman, E.H.Y. Cheng, S.J. Korsmeyer, Proapoptotic BAX and BAK control multiple initiator caspases, EMBO Reports 6 (2005) 379–385.
[65] C. Chiu, L. Lee, Y. Li, Y. Chen, Y. Lu, Y. Li, H. Wang, J. Chang, A. Cheng, Grp78 as a therapeutic target for refractory head–neck cancer with CD24− CD44+ stemness phenotype, Canc. Gene Ther. 20 (2013) 606–615.
[66] Y.-Y. Huang, L.-J. Pu, L.-L. Song, L.-Y. Ma, H. Liu, C.-C. Jiang, Knockdown of GRP78 enhances cell death by cisplatin and radiotherapy in nasopharyngeal cells, Anti Canc. Drugs 27 (2016) 726–733.
[67] H. Ju, P. Arumugam, J. Lee, J.M. Song, Impact of environmental pollutant cadmium on the establishment of a cancer stem cell population in breast and hepatic cancer, ACS Omega 2 (2017) 563–572.
[68] Y.K. Tak, P.K. Naoghare, E. Han, J.M. Song, VEGF inhibitor (Iressa) arrests histone deacetylase expression: single-cell cotransfection imaging cytometry for multi-target-multi-drug analysis, J. Cell. Physiol. 226 (2011) 2115–2122.
[69] J. Ahn, T. Xia, H. Konno, K. Konno, P. Ruiz, G.N. Barber, Inflammation-driven carcinogenesis is mediated through STING, Nat. Commun. 5 (2014) 5166.
[70] P. Arumugam, A. Samson, J. Ki, J.M. Song, Knockdown of clusterin alters mitochondrial dynamics, facilitates necrosis in camptothecin-induced cancer stem cells, Cell Biol. Toxicol. 33 (2017) 307–321.